

# Mercury Telluride Quantum Dot Based Phototransistor Enabling High-Sensitivity Room-Temperature Photodetection at 2000 nm

Mengyu Chen,<sup>†,⊥</sup> Haipeng Lu,<sup>†,⊥</sup> Nema M. Abdelazim,<sup>‡,⊥</sup> Ye Zhu,<sup>§</sup> Zhen Wang,<sup>||</sup> Wei Ren,<sup>||</sup> Stephen V. Kershaw,<sup>\*,‡,ID</sup> Andrey L. Rogach,<sup>‡,ID</sup> and Ni Zhao<sup>\*,†,ID</sup>

<sup>†</sup>Department of Electronic Engineering and <sup>||</sup>Department of Mechanical and Automation Engineering, The Chinese University of Hong Kong, Shatin, New Territories, Hong Kong S. A. R.

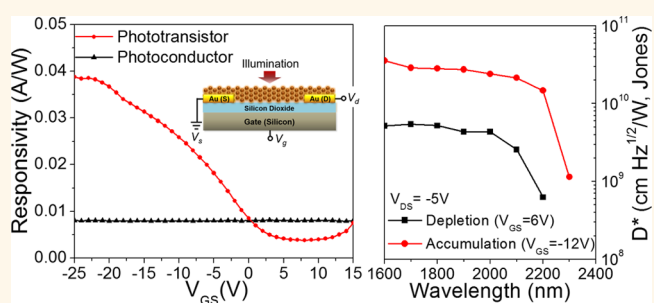
<sup>‡</sup>Department of Physics and Materials Science and Centre for Functional Photonics (CFP) City University of Hong Kong, Kowloon, Hong Kong S. A. R.

<sup>\*</sup>Department of Applied Physics, The Hong Kong Polytechnic University, Kowloon, Hong Kong S. A. R.

## S Supporting Information

**ABSTRACT:** Near-to-mid-infrared photodetection technologies could be widely deployed to advance the infrastructures of surveillance, environmental monitoring, and manufacturing, if the detection devices are low-cost, in compact format, and with high performance. For such application requirements, colloidal quantum dot (QD) based photodetectors stand out as particularly promising due to the solution processability and ease of integration with silicon technologies; unfortunately, the detectivity of the QD photodetectors toward longer wavelengths has so far been low. Here we overcome this performance bottleneck through synergistic efforts between synthetic chemistry and device engineering. First, we developed a fully automated aprotic solvent, gas-injection synthesis method that allows scalable fabrication of large sized HgTe QDs with high quality, exhibiting a record high photoluminescence quantum yield of 17% at the photoluminescence peak close to 2.1  $\mu\text{m}$ . Second, through gating a phototransistor structure we demonstrate room-temperature device response to reach  $>2 \times 10^{10} \text{ cm Hz}^{1/2} \text{ W}^{-1}$  (at 2 kHz modulation frequency) specific detectivity beyond the 2  $\mu\text{m}$  wavelength range, which is comparable to commercial epitaxial-grown photodetectors. To demonstrate the practical application of the QD phototransistor, we incorporated the device in a carbon monoxide gas sensing system and demonstrated reliable measurement of gas concentration. This work represents an important step forward in commercializing QD-based infrared detection technologies.

**KEYWORDS:** quantum dot, phototransistor, near-to-mid infrared, photodetection, gas sensing



Near-to-mid-infrared (IR) photodetection technologies have the potential to revolutionize the infrastructures of surveillance and manufacturing by enabling military or civil night vision,<sup>1,2</sup> environmental gas monitoring,<sup>3</sup> and chemical spectroscopic analysis.<sup>4</sup> However, current commercial IR photodetectors, particularly those with beyond 2000 nm spectral response, rely on expensive and size-limited epitaxial growth processes that are not compatible with silicon wafer technologies.<sup>5</sup> Especially, most of the photodetectors operating in this wavelength range required bulky low-temperature operation units such as thermoelectric cooling (TEC) or liquid nitrogen cooling to achieve the desired signal-to-noise ratio (e.g., InGaAs,<sup>6</sup> HgCdTe,<sup>7,8</sup> InSb<sup>9</sup>). Although some photo-

conductive photodetectors (e.g., PbS)<sup>10</sup> can be operated at room temperature with a decent detectivity ( $\sim 1 \times 10^{11}$  Jones (or  $\text{cm}\cdot\text{Hz}^{1/2}/\text{W}$  in SI units)), their response speed is rather low. Therefore, a low-cost, room-temperature-operated, and sensitive IR photodetector is highly desired in compact or miniaturized photodetection systems for portable imagers and spectrometers or sensor network applications.

**Received:** February 12, 2017

**Accepted:** May 19, 2017

**Published:** May 19, 2017



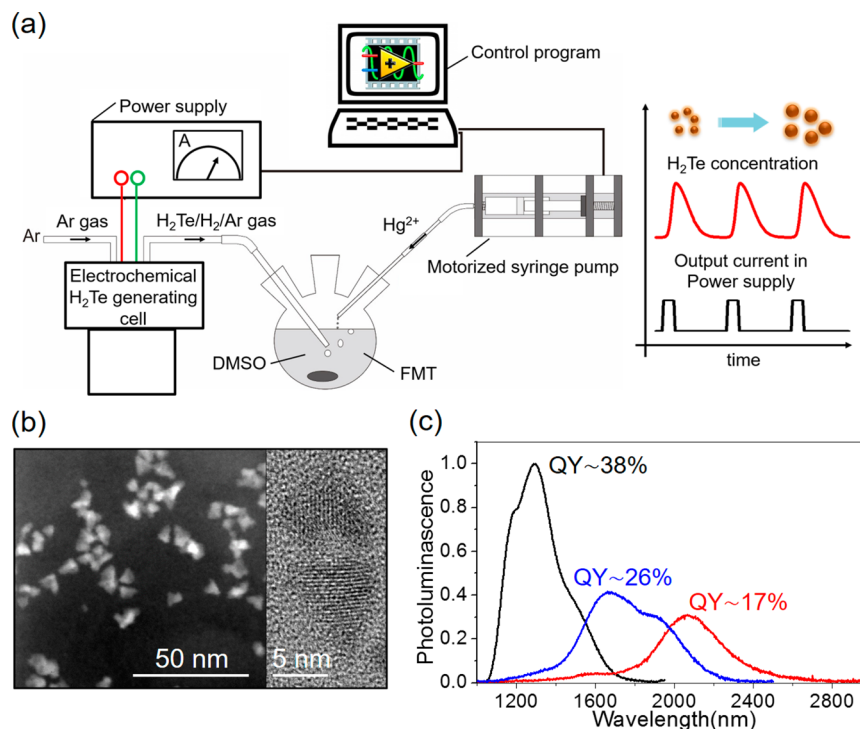


**Figure 1.** (a) Schematic setup of aprotic solvent, gas-injection synthesis setup for  $\text{HgTe}$  QDs. (b) Annular-dark-field scanning TEM image and typical HRTEM image of the  $\text{HgTe}$  QDs (cast from toluene/dodecanethiol ligand solution and with a PL peak at about 2200 nm). (c) PL spectra of  $\text{HgTe}$  QDs with the solution PLQY values indicated.

Colloidal  $\text{HgTe}$  quantum dots (QDs), with a spectral response spanning almost the entire near-to-mid-IR range,<sup>11–13</sup> are a promising material candidate for the new-generation photodetectors. However, long-wavelength  $\text{HgTe}$  QD based photodetectors have so far exhibited a rather low room-temperature specific detectivity ( $<10^9$  Jones (or  $\text{cm Hz}^{1/2} \text{W}^{-1}$  in SI units)).<sup>14</sup> The performance limitation of  $\text{HgTe}$  QD based photodetectors mainly stems from two reasons. The first one is related to synthetic difficulties in producing high-quality QDs. The widely used hot-injection method combined with organic solvent growth can effectively extend the absorption edge of  $\text{HgTe}$  QDs to the long-wavelength IR range;<sup>13,15</sup> however, rapid growth at high temperatures can result in a large amount of surface recombination centers, which significantly reduces the photoluminescence quantum yield (PLQY)<sup>16</sup> of the QDs. On the other hand, room-temperature aqueous methods have been shown to allow high PLQY, but they are in practice limited to QD diameters of typically less than 5 nm (*i.e.*, with emission  $\leq 1800$  nm)<sup>17</sup> unless combined with a subsequent heating stage to promote QD enlargement by Ostwald ripening.<sup>18</sup> It should be noted however that Ostwald ripening, particularly for aqueous solvent based systems, when pushed beyond certain limits can also have limitations such as poor QD size control and low PLQY.<sup>19</sup> The second reason for the poor performance of  $\text{HgTe}$  QD photodetectors is their unoptimized device structures. Due to the narrow band gap of  $\text{HgTe}$  QDs, it is difficult to find a matching material that can form a type II heterojunction with the QD film; therefore, nearly all the QD photodetectors operated beyond the 2000 nm spectral range are based on a photoconductor structure,<sup>12–14</sup> rather than a photodiode structure, as the former has little requirement on energy level alignment. Unfortunately, the photoconductor structure offers very limited control on the distribution and transport of charge carriers in the semi-

conductor layer. This limitation could be overcome by adding a “gating bias” through a field-effect transistor (FET) structure. FET structures have previously been used to characterize doping polarity and charge carrier mobility of  $\text{HgTe}$  QD<sup>14</sup> and  $\text{HgSe}$  QD<sup>20</sup> films at low temperatures, but it remained unclear whether a good gating effect can be achieved at room temperature and whether the gated structure could outperform photoconductor structures by enabling tunability in the noise and gain of a photodetector. During the preparation of this paper, we note that a  $\text{HgTe}$  QD/ $\text{MoS}_2$  heterojunction phototransistor with up to  $10^{12}$  Jones detectivity at 2  $\mu\text{m}$  wavelength has been reported;<sup>21</sup> however, the fabrication process of this device is still laborious and cannot be scaled up to produce large-area sensor arrays yet due to the difficulty in patterning the 2D layer.

In this study, we overcome the performance bottleneck of  $\text{HgTe}$  QD photodetectors through synergistic efforts between synthetic chemistry and device engineering. First, we developed a fully automated aprotic solvent, gas-injection synthesis method that allows scalable fabrication of large-sized  $\text{HgTe}$  QDs with high quality, exhibiting a record high PLQY for  $\text{HgTe}$  QDs of 17% at 2080 nm. Second, through layer-by-layer spray-coating of the QD layer we realized a  $\text{HgTe}$  QD based phototransistor with a pronounced gate effect at room temperature. This enabled us to perform a comprehensive parametric analysis on the photodetection performance in different transistor operation regimes, *i.e.*, accumulation *vs* depletion, based on which we successfully improved the room-temperature device response to reach  $>2 \times 10^{10}$  Jones specific detectivity in the 2000 nm wavelength range, which is comparable to the commercial room-temperature-operated, epitaxially grown photodetectors.<sup>10</sup> The temperature-dependent photocurrent and mobility analysis further revealed that the photosensing ability of our phototransistor could be maximized

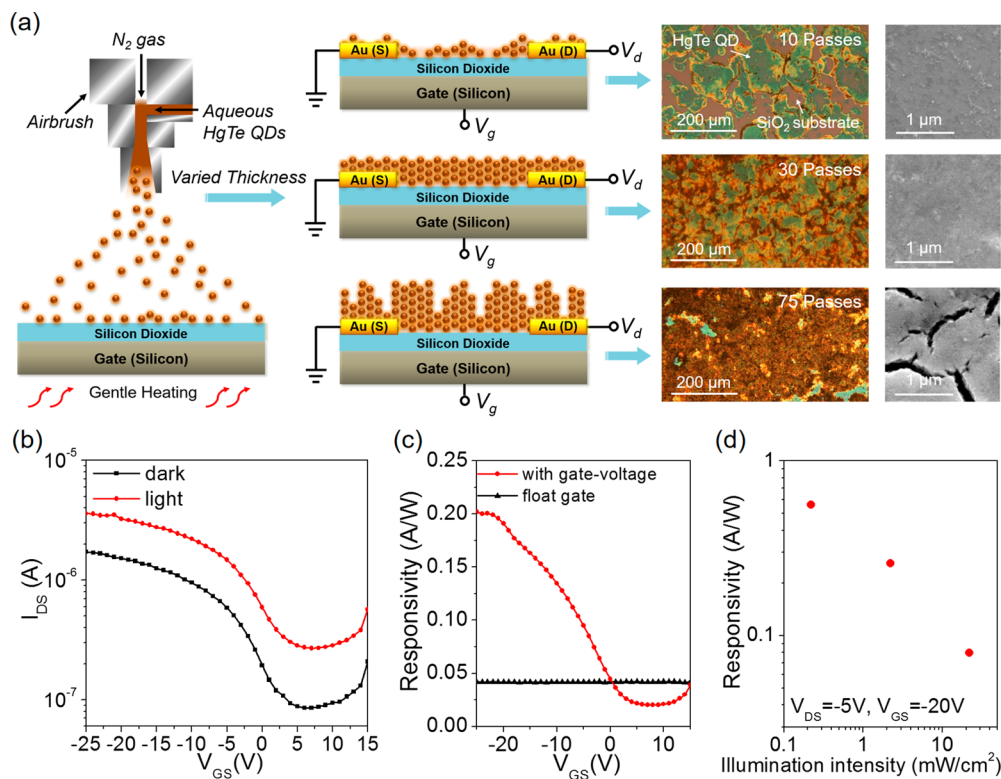


**Figure 2.** (a) Schematics of the spray-coating setup and the aqueous HgTe QD based phototransistor device structures with a range of QD film thicknesses deposited by a series of spray passes. The corresponding optical microscopy and SEM images of the QDs films are shown on the right. (b) Typical transfer characteristics of the aqueous HgTe QD based phototransistor (30 spray passes) under dark and illumination conditions. The curves were measured in a forward scan with  $V_{GS}$  from +15 V to -25 V. (c) Gate-voltage-dependent responsivity of the phototransistor with comparison to the responsivity at floating-gate operation. (d) Light-intensity-dependent responsivity of the phototransistor operated in accumulation mode. Illumination level in (b) and (c): 1550 nm, 4.2 mW/cm<sup>2</sup>. All data are obtained at room temperature (298 K).

at 260 K, an operation temperature that is achievable by integrating the detector with a small-sized single-stage low-current driving TEC unit. To demonstrate the practical application of the QD phototransistor, we incorporated the device in a carbon monoxide gas sensing system, where it exhibited a reliable response to gas concentration fluctuations.

## RESULTS AND DISCUSSION

**QD Synthesis.** The aprotic solvent, gas-injection synthesis (Figure 1a) of HgTe QDs is a modified version of the aqueous synthetic approach where Hg(ClO<sub>4</sub>)<sub>2</sub> reacts with H<sub>2</sub>Te gas in the presence of 1-thioglycerol (TG) as a stabilizing ligand.<sup>17,22,23</sup> In the aqueous synthetic process, aggregation of HgTe QDs starts to prevail when the particle size increases to around 4 nm,<sup>24</sup> hindering further growth of the QDs. In our approach, we introduced two modifications to avoid the aggregation issue. First, we designed a fully automated precursor supply system, which enables us to inject repeated iterations of Hg<sup>2+</sup> salt solution and H<sub>2</sub>Te gas (electrochemically generated) at a Coulombically controlled rate during the prolonged QD growth process. In this manner, by only introducing small amounts of these precursors in each iteration (followed by typically 10–20 min waiting time), we minimize the tendency of QD aggregation and obtain larger sized QDs without recourse to heating and ripening. Second, we choose aprotic dimethyl sulfoxide (DMSO) to replace water as the reaction solvent and paired it with 2-furanmethanethiol (FMT) as the stabilizing ligand.<sup>25,26</sup> FMT is a relatively short ligand

and appears to have a moderate binding affinity for cations both in solution and at the surface of growing QDs. This strikes a reasonable balance between QD stabilization and solvation in DMSO, allowing continued growth of the QDs. DMSO as an aprotic solvent can support less hydrogen bonding than water, being only able to accept hydrogen bonds from acidic hydrogens on the ligand functional groups. This reduces the scope for supramolecular bond formation near the surface of the growing QDs, helping to maintain good access of precursor ions to the surface and extending the size range for room-temperature synthesis. Mercury(II) acetate is used as the Hg precursor because (i) the salt has a good solubility in DMSO and (ii) a moderately hard base (acetate anion) paired with a relatively soft acid cation (Hg<sup>2+</sup>) helps to favor QD formation,<sup>19,27</sup> which possibly assists particularly at larger QD diameters.

Figure 1b shows the transmission electron microscopy (TEM) images of the HgTe QDs, which are well-dispersed and exhibit triangle shapes corresponding to tetrahedra or cube corners. We took three QD samples from different growth stages and examined their PLQY. As shown in Figure 1c, the QY is 38% for the small QDs emitting at 1200 nm, and it is still more than 17% for the large QDs emitting at 2080 nm. These PLQY values are much higher than those obtained from hot-injection synthesis, which are typically in the range of 1–10%.<sup>16</sup> It is worth mentioning that the previous reported aqueous gas-injection/heating ripening combined process also yields a high QY of about 40% for the 1100 nm-emitting QDs; however,

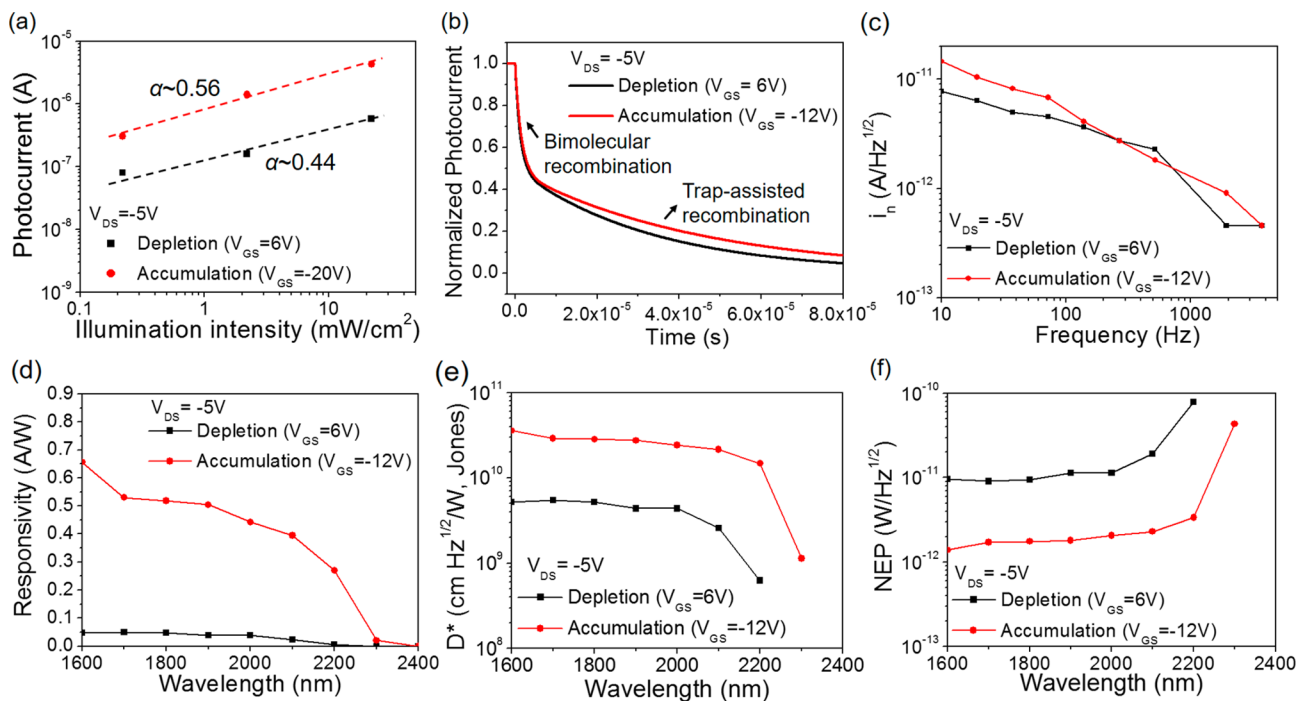


**Figure 3.** (a) Light intensity dependent photocurrent and log–log fit, (b) temporal response, (c) current noise spectral density, (d) wavelength-dependent responsivity, (e) specific detectivity (at 2 kHz), and (f) noise-equivalent power (at 2 kHz) spectra of the HgTe QD based phototransistor (30 spray passes) operated in the depletion mode (black) and accumulation mode (red), respectively. All data were measured at RT (298 K).

when the QDs are grown to emit at 2300 nm, their QY dropped to below 11%.<sup>18</sup> Note that a wavelength-dependent decrease of PLQY occurs naturally for IR QDs. According to Fermi's golden rule, the radiative recombination rate drops significantly with increased emission wavelength, suggesting that the nonradiative recombination will become more dominant for large QDs.<sup>28</sup> Nevertheless, the QY of ~17% is the highest among the reported values for HgTe colloidal QDs that emit beyond 2000 nm.

**Device Fabrication and Performance Characterization.** For device fabrication, the QDs are redispersed in an aqueous solution following a two-step ligand exchange process from FMT to TG. (See **Methods** for the details of the process. Note that DMSO is not a suitable solvent for spray-coating due to its high volatility and toxic solvent fumes.) Fourier transform infrared spectroscopy (FTIR) confirms that the ligand exchange process occurs effectively (Figure S1 in the **Supporting Information**). Next, a bottom-contact/bottom-gate transistor (Figure 2a) is fabricated using a heavily doped silicon substrate as the gate and its oxide surface layer (~300 nm thick SiO<sub>2</sub>) as the gate dielectric. The source and drain contacts are photolithographically patterned gold electrodes. To form the photoactive layer, the aqueous HgTe QD solution is spray-deposited onto the substrate with multiple passes in an ambient environment. The droplet size and spray speed are adjusted such that in each spray pass the QD droplets are sparsely distributed and instantly dried on the substrate surface. The QD film thickness and morphology evolve with the number of spray passes, as shown in the optical microscopy and scanning electron microscopy (SEM) images in Figure 2a. In the initial spray passes, the QD droplets gradually connected with each other but did not yet fully cover the substrate. From the 10th to 30th passes, the QD film started to form a full coverage layer while its thickness continued to grow. When the

pass number further increased to 45 and above, the roughness of the film rapidly increased, accompanied by the emergence of cracks and aggregated particles in the films (Figure 2a and Figure S2b–f in the **Supporting Information**). The morphology change is likely related to redissolution of the QDs deposited in previous passes: as the film becomes thicker, the redissolution sites accumulate. As a result, the film starts to behave like a sponge to absorb solvent from sprayed droplets; since the thickened film releases the solvent far more slowly than the initial thinner layers, the final drying process would leave behind a cracked film.

Subject to the film morphology limitations, the optimal number of spray passes can be determined based on the electrical response of the QD transistors, as shown in Figure S2a in the **Supporting Information**. It can be seen that the gate effect first increases from 10 to 30 spray passes and then decreases after 45 passes, which correlates well with the morphology variation. Since the phototransistor with a 30-pass sprayed QD film exhibits the highest transconductance and on/off ratio, we selected this device configuration for further parametric analysis of photodetection performance. The QD film in this condition typically has a thickness around 80 nm. (SEM image of the cross-section of the film is shown in Figure S3 in the **Supporting Information**.)

The typical dark and light transfer characteristics of the optimized transistor are shown in Figure 2b, and the corresponding gate leakage current of the devices is shown in Figure S4 in the **Supporting Information**. The device can be operated as an ambipolar transistor (Figure S5), but exhibits a predominant p-type behavior, similar to those made with near-IR aqueous HgTe QDs.<sup>29</sup> The suppression of the electron transport may be related to the surface nonstoichiometry<sup>30</sup> and/or the thiolate groups from the negatively charged TG ligands or the OH-terminated SiO<sub>2</sub> surface.<sup>31</sup> At room

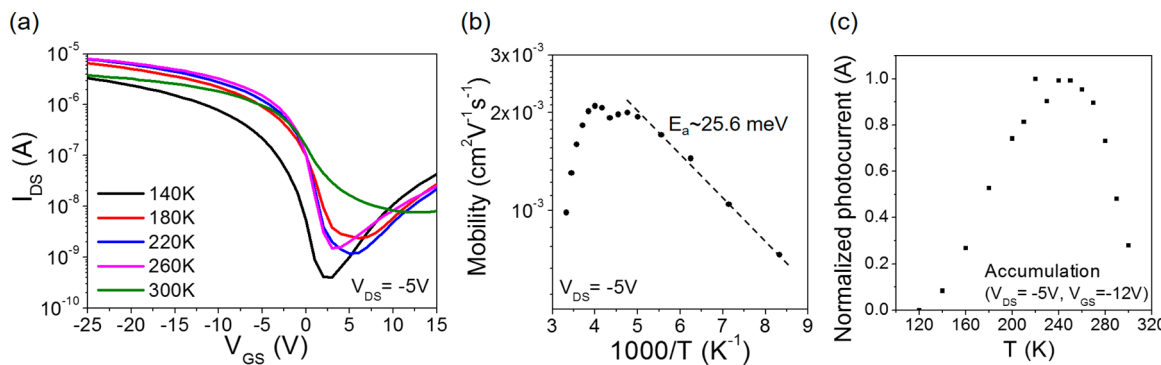


**Figure 4.** (a) Dark transfer characteristics of the HgTe QD phototransistor on a semilogarithmic scale at different temperatures. The curves were obtained in a forward voltage scan with  $V_{GS}$  from +15 V to -25 V. (b) Temperature-dependent hole mobility and the fitting (dashed line) for the low-temperature activation energy. (c) Temperature-dependent normalized photocurrent of the phototransistor operated in accumulation mode (1550 nm, 2.2 mW/cm<sup>2</sup> illumination).

temperature (RT), the on/off ratio of the transistor exceeds 20, indicating a significant gate effect in tuning the carrier density in the active layer. Such a high RT on/off ratio is remarkable for narrow band gap semiconductors,<sup>14,20</sup> and it can be attributed to the lower doping density enabled by the QD synthesis method used here and the suppression of n-type transport, which helps to reduce the recombination current. At accumulation, the charge density is estimated (according to ref 32) to be around 0.49 charge per QD, which is close to 3 orders higher than the charge density in depletion. (See more details in the Supporting Information.)

We now turn to evaluate the photodetection performance of the QD transistor. The commonly used figure-of-merit of a photodetector is specific detectivity or noise-equivalent power (NEP), both of which are determined by the responsivity and noise current of the photodetector. The RT gate-voltage-dependent responsivity of the QD transistor is shown in Figure 2c. As compared to the floating-gate operation (*i.e.*, photoconductor mode), biasing the gate at -25 V (accumulation mode) can raise the responsivity by more than 4 times, while biasing the gate to +6 V (depletion mode) results in a responsivity drop of 50%. Such responsivity variation is likely associated with a trap-filling effect. For instance, in accumulation mode the gate-induced holes help to fill up the hole trap states; consequently, the photogenerated holes can transport in the accumulation layer with a higher mobility, resulting in a shorter transit time for holes in the channel. Our previous study<sup>29</sup> suggests that in the QD photodetectors the responsivity is proportional to the photoconductive gain,  $G$ , and that  $G = \tau_c/\tau_t$ , where  $\tau_c$  is the trap lifetime and  $\tau_t$  is the transit time of the transport carrier. Hence, changing the transit time of the transport carriers (in this case, the holes) will result in variation of the responsivity.

The light intensity dependence of responsivity in the accumulation mode is shown in Figure 2d. Under 0.22 mW/cm<sup>2</sup> illumination, the responsivity reaches 0.56 A/W. The responsivity of the HgTe QD device decreases at high light intensities, suggesting a loss of photoconductive gain. This is due to a transition from trap-assisted charge recombination to band-to-band charge recombination (also referred to as bimolecular recombination) when the amount of photo-generated carriers is increased significantly. As shown in Figure 3a, the power law dependence of the photocurrent ( $I_{ph}$ ) on the light intensity ( $I$ ), *i.e.*,  $I_{ph} \propto I^\alpha$ , can be fitted with  $\alpha \approx 0.56$  in the accumulation mode and  $\alpha \approx 0.44$  in the depletion mode. Both

$\alpha$  values are close to 0.5, corresponding well to a bimolecular recombination dominated process<sup>33</sup> at high light intensities. Note, however, that at low light intensity levels,  $\alpha$  approaches 1; that is, a linear relation between the photocurrent and light intensity is achieved (Figure S7). The transient photocurrent decays (Figure 3b) also suggest that bimolecular recombination dominates at the initial decay stage where charge carrier density is high, while at the later stage the slower trap-assisted recombination process becomes dominant since the charge carrier density becomes low. The effective decay time constants  $\tau_{eff}$  are measured to be about 12.6 and 10.2  $\mu$ s in the accumulation and depletion modes, respectively. Accordingly, the 3 dB bandwidth  $f_{3dB}$  of the QD phototransistors is estimated to be on the order of ~10 kHz based on  $f_{3dB} = 1/(2\pi\tau_{eff})$ .<sup>29</sup>

Noise current is another critical parameter that determines detectivity. It can be seen from Figure 3c that both depletion and accumulation modes follow similar trends of 1/f noise current, suggesting that the noise characteristics are dominated by the nanocrystalline nature of the QD films.<sup>34–36</sup> The depletion mode exhibits lower noise current due to its lower dark current level. It is important to investigate the trade-off between the responsivity  $R$  and noise spectral density  $I_n$  through gate-voltage tuning, in order to achieve the optimized detectivity given by  $D^* = R\sqrt{\text{Area}}/I_n$ . Therefore, the device performances of the optimal phototransistor in both modes were characterized and compared (see Figure S8 in the Supporting Information for noise measurement setup and a detailed discussion).

The wavelength-dependent responsivity spectra of the optimal phototransistor in accumulation mode and depletion mode are compared in Figure 3d. More than 0.4 A/W responsivity is achieved with the accumulation operation just beyond 2000 nm. The responsivity in accumulation mode is 10 times larger than that in depletion mode over the whole spectrum. On the other hand, as suggested in Figure 3c, the noise level in the accumulation mode is only slightly higher than that in the depletion mode. As a result, higher detectivity should be obtained in the accumulation mode. We calculated the wavelength-dependent detectivity ( $D^*$ ) and NEP spectra of the QD-based phototransistor using the noise spectral density at 2 kHz. As shown in Figure 3e, more than  $2 \times 10^{10}$  Jones specific detectivity and lower than  $3 \times 10^{-12}$  W/Hz<sup>1/2</sup> NEP were obtained with the accumulation mode in the 2000–2200 nm spectral range.

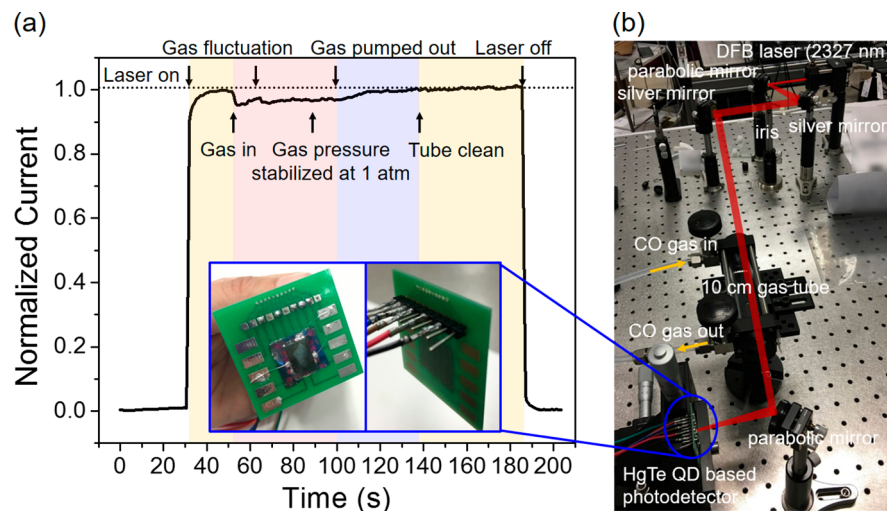


**Figure 5.** (a) Normalized room-temperature photocurrent response of the HgTe QD based phototransistor during the CO gas sensing measurement; (b) photograph of the experimental setup of the gas sensing system. Inset of (a): Photos of the packaged phototransistor.

It is worth emphasizing that all the above characterizations were conducted at room temperature. This responsivity value can be further increased with higher drain- and gate-voltage operation or with the use of smaller channel length and high- $k$  gate dielectrics. The spectral range can be extended to the mid-IR range (e.g., 3000–5000 nm) with modified synthesis conditions. The high-throughput fabrication process, operation tunability, and high room-temperature photoresponse would make this phototransistor a promising competitor to the commercial epitaxially grown IR photodetectors in a similar wavelength range (e.g., the PbS photoconductive detectors sold by Thorlabs, Inc.).<sup>10</sup>

**Temperature-Dependent Characterization.** To explore the optimal operation temperature of the photodetector, we also characterized the temperature-dependent transport properties of the QD transistor. Figure 4a shows the dark transfer characteristics in a semilogarithmic scale (linear scale plot is shown in Figure S9a) measured from 300 to 140 K, based on which the hole mobility as a function of temperature is calculated and plotted in Figure 4b. The mobility first rises with temperature and then reaches a plateau at 260 to 220 K. Considering the low charge carrier mobility in our devices, we believe the charge transport in the QD films is still dominated by charge hopping or tunneling through localized states. Therefore, this “negative temperature coefficient ( $d\mu/dT < 0$ )” phenomenon should not be related to the “band-like” transport commonly seen in inorganic semiconductors<sup>37</sup> nor to the thermal lattice fluctuation-limited charge transport as observed in highly ordered organic semiconductors.<sup>38</sup> Rather, it is likely associated with the thermal contraction or phase transition of the ligands, which may reduce the tunneling barrier between QDs. This phenomenon has also been reported in other QD electronic devices.<sup>39,40</sup> Below 220 K, the mobility decreases as temperature drops, manifesting a thermally activated charge hopping process with an activation energy  $E_a$  of 25.6 meV. We also note that n-type behavior starts to appear at low temperatures. This is because the gating effect in introducing electrons becomes more effective as the amount of thermally generated charge carriers is reduced.

With the increased hole mobility and electron trapping time, the photoconductive gain of the transistor is expected to reach its maximum close to 260 K. As shown in Figure 4c, the

photocurrent at 260 K is 3 times larger than the room-temperature photocurrent, while the dark current is increased by 2 times (Figure S9b in the Supporting Information). Considering the increase of the  $1/f$  noise should be smaller than the increase of the photocurrent current level from 300 to 260 K, the detectivity of our phototransistor may reach its maximum close to 260 K, which can be easily achieved with a small and compact low-current single-stage TEC temperature control unit.<sup>41</sup>

**Gas Sensing Application.** Finally, to demonstrate the potential application of the HgTe QD based phototransistor in gas sensing applications, we integrated the device into a typical gas sensing measurement system (tunable diode laser absorption spectroscopy)<sup>42–44</sup> as the photodetection unit for carbon monoxide (CO) detection. A photograph of the system is shown in Figure 5b, where a laser light (Nanoplus, 2.3  $\mu$ m distributed feedback laser) with its wavelength tuned to the R(10) line of CO<sup>45,46</sup> (~2327 nm) is directed through a 10 cm long gas cell and then focused onto the phototransistor mounted on a printed circuit board (inset of Figure 5a). During the measurement, the gas cell is first ventilated with a nitrogen/CO gas mixture (0.9% CO concentration) at a controlled pressure (1 bar) and then evacuated into a vacuum. The corresponding current response of the phototransistor is recorded as a function of time. The normalized current response during the whole measurement process is shown in Figure 5a. The phototransistor has a sharp response to the illumination at the moment of being turned on/off. When CO is introduced into the cell, the photocurrent drops immediately due to the light absorption by CO. We note that the photocurrent is sensitive to the concentration variation of CO: both the gas fluctuation during ventilation and the pump-out process of CO can be resolved. On the basis of the photocurrent drop at the stabilized gas pressure, the absorption coefficient of CO at 2327 nm is measured to be  $3.57 \times 10^{-3}$   $\text{cm}^{-1}$ , which is close to the theoretical value of  $3.60 \times 10^{-3}$   $\text{cm}^{-1}$  calculated from the HITRAN database<sup>45</sup> at room temperature, at atmospheric pressure, and with a CO gas concentration of 0.9%.

## CONCLUSION

In summary, we have demonstrated a HgTe QD based photodetector that exhibits above  $2 \times 10^{10}$  Jones specific detectivity beyond a 2  $\mu\text{m}$  wavelength range at room-temperature operation. Several key elements to enable such high performance are discussed. First, the fully automated aprotic solvent, gas-injection synthesis allows well-controlled fabrication of high-quality HgTe QDs. Second, the layer-by-layer spray-coating process enables thickness optimization of the QD layer to realize a gating effect in the transistor structure at room temperature. Finally, bias-dependent photodetection parameters, including responsivity, noise, and bandwidth, are analyzed to reveal the optimal operation window for high detectivity. The successful implementation of the QD photodetector in a harmful gas sensing system demonstrates its promising potential in enabling portable sensing devices or sensor networks. Our findings shed light on the fundamental elements that enable commercialization of QD-based infrared detection technologies.

## METHODS

**HgTe QD Synthesis.** The electrochemical cell generated a mixture of  $\text{H}_2$  and  $\text{H}_2\text{Te}$  gases via electrolysis of a phosphoric acid solution using a Te anode and Pt cathode. The mixture of gases was passed over into the reaction flask in a steady stream of argon gas. The electrolysis current was supplied by a power supply unit operating in current regulated mode. Additional  $\text{Hg}^{2+}$  salt solution in DMSO could be added at later stages in the synthesis if required via a syringe pump. The power supply unit and the syringe pump were controlled by a computer running a LabView program. The reaction was carried out under argon in a 500 mL three-necked reaction flask with a magnetic stirrer.

Typically, 300 mL of DMSO containing 380 mg of mercury acetate and 0.24 mL of 2-furanmethanethiol were added to the reaction flask and stirred while deaerating for an hour in a flow of Ar gas. The same stream of Ar gas was first passed through the electrolysis cell in series with the reaction cell. During the reaction,  $\text{H}_2\text{Te}$  is generated by passing 50 mA of current for 20 min through the electrolysis cell, and then the current was turned off and the gas allowed to fully absorb and react in the main reaction flask for 30 min. A few-milliliter aliquot may then be taken from the flask, and its optical properties (PL, absorption, hydrodynamic size) were measured to determine the QD size and QD concentration. This process was repeated many times by the control program to advance the QD growth. Up to 50 such increments typically result in material emitting at just over 2000 nm. Aliquots (usually a few milliliters) were removed automatically at various increment intervals using a peristaltic pump based sampling system.

**Ligand Exchange and Precipitation Process.** The purpose of each of the three different solvent/ligand stages described below are initial room-temperature growth in DMSO with FMT ligand to obtain improved QD surface quality; transfer to tetrachloroethylene (TCE) with dodecanethiol (DDT) ligand for spectroscopy and characterization and to move out of DMSO, which has too high a boiling point for spin-coating or spray-coating film formation; and transfer to water and 1-thioglycerol (1-TG), where the ligand length is short and improves film conductivity (closer QD packing) and spray coating is possible.

QDs prepared in DMSO with FMT ligands were transferred into TCE solution, and the FMT was replaced with DDT ligands. DMSO is strongly absorbing in the IR, and FMT is not compatible with the TCE solvent. After ligand exchange the solution was purified several times to reduce the DDT concentration to the minimum level required to stabilize the QDs in TCE. For the spray fabrication of devices, the QDs have been further transferred from a TCE/DDT solution into water with 1-TG replacing the DDT ligands. The QDs were initially transferred into a 5:1 tetrahydrofuran (THF)/*n*-methylpyrrolidone solution to facilitate the displacement of the

DDT ligand in favor of the 1-TG when transferring the QDs into aqueous solution. After the QDs have partitioned into the aqueous phase, any organically soluble content was removed by washing the water-based solution with toluene. Excess 1-TG was removed by precipitating the aqueous phase with acetonitrile followed by centrifugation. The dried precipitate was then redissolved in water and used for spray-coating deposition.

**Device Fabrication.** The silicon wafers with prepatterned gold interdigitated electrodes (15 periods, 1 mm long, and 5  $\mu\text{m}$  spacing) were prepared photolithographically, using metal thermal deposition followed by a lift-off process. After 100 s of oxygen plasma treatment, the samples were heated gently on a 55 °C hot plate for spray deposition in an ambient environment. The airbrush (Tamiya SparMax SX0.3D) with a nozzle size of 0.3 mm was fixed 11.4 cm above the hot plate. The flow rate of the HgTe QD solution was controlled by the gas pressure (0.3–0.5 bar). The film samples were washed out with a 1:2 methanol/acetonitrile solution to remove residual  $\text{Na}^+$  ions and then encapsulated by glass slides under a nitrogen atmosphere in a glovebox. The optical sensing area of the phototransistor is  $2.45 \times 10^{-3} \text{ cm}^2$ .

**Characterization.** Absolute PLQY values in the NIR up to 1600 nm were determined using an integrating sphere fitted to an Edinburgh Instruments FLS920P fluorescence spectrometer. Typically, aliquots from the first 3–4 reaction loops fell in this emission range. For longer wavelength samples, relative PLQY values were estimated by comparing the integrated PL peaks normalized by the absorption at the excitation wavelength (880 nm) using the previous short-wavelength-emitting aliquots as the QY references. Concentrations were adjusted such that they were close to the same for all the samples in the relative PLQY determinations.

The SEM imaging was carried out on an FEI Quanta 400 FEG microscope. The FTIR spectra were measured with a Bruker Vertex 70 FTIR spectrometer. TEM observations were conducted on a JEOL JEM-2100F TEM/STEM operated at 200 kV, located at the University Research Facility in Materials Characterization and Device Fabrication (UMF), Centre for Electron Microscopy, the Hong Kong Polytechnic University.

The current–voltage characteristics were measured with a Keithley 2612 source meter. The transfer characteristics scans were measured in a pulse mode (pulse width = 100 ms, sampling interval = 1–2 s), and this condition gives highly reproducible data when we do multiple *I*–*V* scans. For other measurements, the time required for stabilization is about a few seconds to 10 s after changing the gate voltage. Note that this value is highly sensitive to the QD quality as well as the interface property. The light current was generated by illuminating the device with a Newport LQD1550E 5 mW 1550 nm laser. The light intensity dependent properties were calibrated with the same setup with a NIR absorptive filter. The wavelength-dependent responsivity was measured with a Keithley 2612 source meter under monochromatic illumination generated by passing the light beam from a 250 W quartz tungsten halogen lamp into a Newport 74125 Oriel Cornerstone 260 1/4 m monochromator. The optical power density was measured to be about 1 mW/cm<sup>2</sup> at  $\lambda = 800$  nm. The light passed through a 1500 nm long pass filter and was focused by two  $\text{CaF}_2$  lenses onto the samples. A Hamamatsu P5968-200 InSb photovoltaic detector was used to calibrate the optical power density. The reference InSb photodetector was operated at 80 K with liquid nitrogen cooling.

For transient photocurrent measurement, all devices were biased with a Keithley 2612 source meter and illuminated by a function generator (Agilent 33210A) modulated Newport LQD1550E laser with an 11 Hz repetition frequency. The resulting photocurrent was amplified by a Femto DHPCA-100 high-speed current amplifier and recorded with a Tektronix TDS 3014C oscilloscope.

For noise current spectral density measurement, devices were sealed in a metal shielding box with battery biased source–drain and gate–drain voltages. A lock-in amplifier (Stanford Research 830) was connected in series to the test device to measure the noise current at different frequencies with measurement units of A/Hz<sup>1/2</sup>. The impedance of the lock-in amplifier was 1 k $\Omega$ , which was much smaller

than the source–drain resistance of the device (larger than  $1\text{ M}\Omega$  even where a gate voltage was applied).

## ASSOCIATED CONTENT

### S Supporting Information

Additional figures. The Supporting Information is available free of charge on the ACS Publications website at DOI: 10.1021/acsnano.7b00972.

(PDF)

## AUTHOR INFORMATION

### Corresponding Authors

\*E-mail: skershaw@cityu.edu.hk.

\*E-mail: nzhao@ee.cuhk.edu.hk.

### ORCID

Ye Zhu: 0000-0002-5217-493X

Wei Ren: 0000-0001-6681-593X

Stephen V. Kershaw: 0000-0003-0408-4902

Andrey L. Rogach: 0000-0002-8263-8141

Ni Zhao: 0000-0002-1536-8516

### Author Contributions

<sup>†</sup>M. Chen, H. Lu, and N. M. Abdelazim contributed equally to this work.

### Notes

The authors declare no competing financial interest.

## ACKNOWLEDGMENTS

We gratefully acknowledge funding from the Research Grants Council of Hong Kong S.A.R. through the Early Career Scheme (Project CUHK439013), General Research Funds (Project CityU 11302114), and internal grant (Project 9610350) of City University of Hong Kong. Y.Z. was financially supported by The Hong Kong Polytechnic University grant (Project No. 1-ZE6G). Y.Z. thanks Dr. Lu Wei for optimizing the JEOL JEM-2100F microscope.

## REFERENCES

- (1) Hansen, M. P.; Malchow, D. S. Overview of SWIR Detectors, Cameras, and Applications. *Proc. SPIE* **2008**, 6369, 69390I–1–69390I-11.
- (2) Schreiner, K. Night Vision: Infrared Takes to The Road. *IEEE Comput. Graph. Appl.* **1999**, 19, 6–10.
- (3) Stepanov, E. V.; Kouznetsov, A. I.; Zyrianov, P. V.; Plotnichenko, V. G.; Selivanov, Yu. G. Multicomponent Fiber-Optical Gas Sensor based on MIR Tunable Diode Lasers. *Infrared Phys. Technol.* **1996**, 37, 149–153.
- (4) Bacon, C. P.; Mattley, Y.; DeFrece, R. Miniature Spectroscopic Instrumentation: Applications to Biology and Chemistry. *Rev. Sci. Instrum.* **2004**, 75, 1–16.
- (5) Rogalski, A. Recent Progress in Infrared Detector Technologies. *Infrared Phys. Technol.* **2011**, 54, 136–154.
- (6) Thorlabschina.cn. InGaAs Amplified Photodetector with Thermoelectric Cooler. Retrieved April 7, 2017, from [https://www.thorlabschina.cn/newgroupage9.cfm?objectgroup\\_id=5713](https://www.thorlabschina.cn/newgroupage9.cfm?objectgroup_id=5713).
- (7) Thorlabschina.cn. HgCdTe (MCT) Amplified Photodetector. Retrieved April 7, 2017, from [https://www.thorlabschina.cn/newgroupage9.cfm?objectgroup\\_id=2907](https://www.thorlabschina.cn/newgroupage9.cfm?objectgroup_id=2907).
- (8) VIGO SYSTEM S.A. - PVI-2TE. Retrieved December 30, 2016, from <http://www.vigo.com.pl/products/infrared-detectors/Photovoltaic-Detectors/pvi-2te-series>.
- (9) InSb Photovoltaic Detectors | Hamamatsu Photonics. Retrieved December 30, 2016, from <https://www.hamamatsu.com/eu/en/product/category/3100/4007/4140/index.html>.
- (10) Thorlabschina.cn. (2017). *IR Photoconductive Detectors*. Retrieved May 1, 2017, from [https://www.thorlabs.com/newgroupage9.cfm?objectgroup\\_id=6479](https://www.thorlabs.com/newgroupage9.cfm?objectgroup_id=6479).
- (11) Böberl, M.; Kovalenko, M. V.; Gamerith, S.; List, E. J. W.; Heiss, W. Inkjet-Printed Nanocrystal Photodetectors Operating up to  $3\text{ }\mu\text{m}$  Wavelengths. *Adv. Mater.* **2007**, 19, 3574–3578.
- (12) Keuleyan, S.; Lhuillier, E.; Brajuskovic, V.; Guyot-Sionnest, P. Mid-Infrared HgTe Colloidal Quantum Dot Photodetectors. *Nat. Photonics* **2011**, 5, 489–493.
- (13) Keuleyan, S. E.; Guyot-Sionnest, P.; Delerue, C.; Allan, G. Mercury Telluride Colloidal Quantum Dots: Electronic Structure, Size-Dependent Spectra, and Photocurrent Detection up to  $12\text{ }\mu\text{m}$ . *ACS Nano* **2014**, 8, 8675–8682.
- (14) Lhuillier, E.; Keuleyan, S.; Zolotavin, P.; Guyot-Sionnest, P. Mid-Infrared HgTe/As<sub>2</sub>S<sub>3</sub> Field Effect Transistors and Photodetectors. *Adv. Mater.* **2013**, 25, 137–141.
- (15) Keuleyan, S.; Lhuillier, E.; Guyot-Sionnest, P. Synthesis of Colloidal HgTe Quantum Dots for Narrow Mid-IR Emission and Detection. *J. Am. Chem. Soc.* **2011**, 133, 16422–16424.
- (16) Keuleyan, S.; Kohler, J.; Guyot-Sionnest, P. Photoluminescence of Mid-Infrared HgTe Colloidal Quantum Dots. *J. Phys. Chem. C* **2014**, 118, 2749–2753.
- (17) Kershaw, S. V.; Susha, A. S.; Rogach, A. L. Narrow Bandgap Colloidal Metal Chalcogenide Quantum Dots: Synthetic Methods, Heterostructures, Assemblies, Electronic and Infrared Optical Properties. *Chem. Soc. Rev.* **2013**, 42, 3033–3087.
- (18) Kovalenko, M. V.; Kaufmann, E.; Pachinger, D.; Roither, J.; Huber, M.; Stangl, J.; Hesser, G.; Schäffler, F.; Heiss, W. Colloidal HgTe Nanocrystals with Widely Tunable Narrow Band Gap Energies: From Telecommunications to Molecular Vibrations. *J. Am. Chem. Soc.* **2006**, 128, 3516–3517.
- (19) Jing, L.; Kershaw, S. V.; Li, Y.; Huang, X.; Li, Y.; Rogach, A. L.; Gao, M. Aqueous Based Semiconductor Nanocrystals. *Chem. Rev.* **2016**, 116, 10623–10730.
- (20) Lhuillier, E.; Scarafaglio, M.; Hease, P.; Nadal, B.; Aubin, H.; Xu, X. Z.; Lequeux, N.; Patriarche, G.; Ithurris, S.; Dubertret, B. Infrared Photodetection Based on Colloidal Quantum-Dot Films with High Mobility and Optical Absorption up to THz. *Nano Lett.* **2016**, 16, 1282–1286.
- (21) Huo, N.; Gupta, S.; Konstantatos, G. MoS<sub>2</sub>-HgTe Quantum Dot Hybrid Photodetectors beyond  $2\text{ }\mu\text{m}$ . *Adv. Mater.* **2017**, 1606576, 1–5.
- (22) Rogach, A.; Kershaw, S.; Burt, M.; Harrison, M.; Kornowski, A.; Eychmüller, A.; Weller, H. Colloidally Prepared HgTe Nanocrystals with Strong Room-Temperature Infrared Luminescence. *Adv. Mater.* **1999**, 11, 552–555.
- (23) Harrison, M. T.; Kershaw, S. V.; Burt, M. G.; Eychmüller, A.; Weller, H.; Rogach, A. L. Wet Chemical Synthesis and Spectroscopic Study of CdHgTe Nanocrystals with Strong Near-Infrared Luminescence. *Mater. Sci. Eng., B* **2000**, B69–70, 355–360.
- (24) Kershaw, S. V.; Rogach, A. L. Infrared Emitting HgTe Quantum Dots and Their Waveguide and Optoelectronic Devices. *Z. Phys. Chem.* **2015**, 229, 23–64.
- (25) Nijssen, L. M.; Visscher, C. A.; Maarse, H.; Willemse, L. C.; Boelens, M. H. *Volatile Compounds in Food: Qualitative and Quantitative Data*, 7th ed.; TNO Nutrition and Food Research Institute: Zeist, The Netherlands, 1996; pp 72.1–72.23.
- (26) Blank, I.; Sen, A.; Grosch, W. Aroma Impact Compounds of Arabica and Robusta Coffee. Qualitative and Quantitative Investigations. *ASIC. 14e Colloque. San Francisco* **1991**, 117–129.
- (27) Izquierdo, E.; Robin, A.; Keuleyan, S.; Lequeux, N.; Lhuillier, E.; Ithurria, S. Strongly Confined HgTe 2D Nanoplatelets as Narrow Near Infrared Emitters. *J. Am. Chem. Soc.* **2016**, 138, 10496–10601.
- (28) Hens, Z.; Moreels, I. Light Absorption by Colloidal Semiconductor Quantum Dots. *J. Mater. Chem.* **2012**, 22, 10406–10415.
- (29) Chen, M.; Yu, H.; Kershaw, S. V.; Xu, H.; Gupta, S.; Hetsch, F.; Rogach, A. L.; Zhao, N. Fast, Air-Stable Infrared Photodetectors Based on Spray-Deposited Aqueous HgTe Quantum Dots. *Adv. Funct. Mater.* **2014**, 24, 53–59.

- (30) Oh, S. J.; Berry, N. E.; Choi, J.-H.; Gaulding, E. A.; Lin, H.; Paik, T.; Diroll, B. T.; Muramoto, S.; Murray, C. B.; Kagan, C. R. Designing High-Performance PbS and PbSe Nanocrystal Electronic Devices Through Stepwise, Post-Synthesis, Colloidal Atomic Layer Deposition. *Nano Lett.* **2014**, *14*, 1559–1566.
- (31) Lee, S.; Koo, B.; Shin, J.; Lee, E.; Park, H.; Kim, H. Effects of Hydroxyl Groups in Polymeric Dielectrics on Organic Transistor Performance. *Appl. Phys. Lett.* **2006**, *88*, 162109.
- (32) Liu, Y.; Tolentino, J.; Gibbs, M.; Ihly, R.; Perkins, C. L.; Liu, Y.; Crawford, N.; Hemminger, J. C.; Law, M. PbSe Quantum Dot Field-Effect Transistors with Air-Stable Electron Mobilities above  $7 \text{ cm}^2 \text{ V}^{-1} \text{ s}^{-1}$ . *Nano Lett.* **2013**, *1*, 1578–1587.
- (33) Bube, R. H. *Photoconductivity of Solids*; John Wiley and Sons, Inc., New York, 1960; Vol. 3.
- (34) Lhuillier, E.; Keuleyan, S.; Rekemeyer, P.; Guyot-Sionnest, P. Thermal Properties of Mid-Infrared Colloidal Quantum Dot Detectors. *J. Appl. Phys.* **2011**, *110*, 033110.
- (35) Liu, H.; Lhuillier, E.; Guyot-Sionnest, P. 1/f Noise in Semiconductor and Metal Nanocrystal Solids. *J. Appl. Phys.* **2014**, *115*, 154309.
- (36) Lai, Y.; Li, H.; Kim, D. K.; Diroll, B. T.; Murray, C. B.; Kagan, C. R. Low-Frequency (1/f) Noise in Nanocrystal Field-Effect Transistors. *ACS Nano* **2014**, *8*, 9664–9672.
- (37) Lee, J.-S.; Kovalenko, M. V.; Huang, J.; Chung, D. S.; Talapin, D. V. Band-Like Transport, High Electron Mobility and Photoconductivity in All-Inorganic Nanocrystal Arrays. *Nat. Nanotechnol.* **2011**, *6*, 348–352.
- (38) Sakanoue, T.; Sirringhaus, H. Band-Like Temperature Dependence of Mobility in A Solution-Process Organic Semiconductor. *Nat. Mater.* **2010**, *9*, 736–740.
- (39) Ju, T.; Graham, R. L.; Zhai, G.; Rodriguez, Y. W.; Breeze, A. J.; Yang, L.; Alers, G. B.; Carter, S. A. High Efficiency Mesoporous Titanium Oxide PbS Quantum Dot Solar Cells at Low Temperature. *Appl. Phys. Lett.* **2010**, *97*, 043106.
- (40) Loef, R.; Houtepen, A. J.; Talgorn, E.; Schoonman, J.; Goossens, A. Temperature Dependence of Electron Transport in CdSe Quantum Dot Films. *J. Phys. Chem. C* **2009**, *113*, 15992–15996.
- (41) DiSalvo, F. J. Thermoelectric Cooling and Power Generation. *Science* **1999**, *285*, 703–706.
- (42) Werle, P.; Slemp, F.; Maurer, K.; Kormann, R.; Mücke, R.; Janker, B. Near- and Mid-Infrared Laser-Optical Sensors for Gas Analysis. *Opt. Las. Eng.* **2002**, *37*, 101–114.
- (43) Spearin, R. M.; Ren, W.; Jeffries, J. B.; Hanson, R. K. Multi-Band Infrared CO<sub>2</sub> Absorption Sensor for Sensitive Temperature and Species Measurements in High-Temperature Gases. *Appl. Phys. B: Lasers Opt.* **2014**, *116*, 855–865.
- (44) Ren, W.; Dames, E.; Hyland, D.; Davidson, D. F.; Hanson, R. K. Shock Tube Study of Methanol, Methyl Formate Pyrolysis: CH<sub>3</sub>OH and CO Time-History Measurements. *Combust. Flame* **2013**, *160*, 2669–2679.
- (45) Rothman, L. S.; Gordon, I. E.; Barbe, A.; Benner, D. C.; Bernath, P. F.; Birk, M.; Boudon, V.; Brown, L. R.; Campargue, A.; Champion, J.-P.; Chance, K.; Coudert, L. H.; Dana, V.; Devi, V. M.; Fally, S.; Flaud, J.-M.; Gamache, R. R.; Goldman, A.; Jacquemart, D.; Kleiner, I.; et al. The HITRAN 2008 Molecular Spectroscopic Database. *J. Quant. Spectrosc. Radiat. Transfer* **2009**, *110*, 533–572.
- (46) Li, Z.; Wang, Z.; Wang, C.; Ren, W. Optical Fiber Tip-Based Quartz-Enhanced Photoacoustic Sensor for Trace Gas Detection. *Appl. Phys. B: Lasers Opt.* **2016**, *122*, 147.